Cyclone–Anticyclone Asymmetry Organizes Local Energy Transfers during Mixed Layer Instability

Han Bing, Xiaolei Li, Lingling Xie, and Yang Zhang

College of Oceanography and Meteorology, Guangdong Ocean University, Zhanjiang, China

The paper is a non-peer reviewed preprint submitted to EarthArXiv.

Han Bing: hanbing060066@163.com Xiaolei Li: xli@gdou.edu.cn Lingling Xie: xiell@gdou.edu.cn Yang Zhang: zhangyang_gdou@126.com

Cyclone–Anticyclone Asymmetry Organizes Local Energy Transfers during Mixed Layer Instability

Han Bing a , Xiaolei Li a , Lingling Xie a , and Yang Zhang a

a *College of Oceanography and Meteorology, Guangdong Ocean University, Zhanjiang, China*

Corresponding author: Yang Zhang, zhangyang_gdou@126.com

ABSTRACT: Mixed layer instability (MLI) generates submesoscale fronts, filaments, and eddies, yet how cyclone–anticyclone asymmetry shapes the spatial distribution of energy transfers remains unclear. Ageostrophic convergence during frontal sharpening amplifies cyclonic vorticity, first producing a positively skewed vorticity distribution and later a cyclonically biased flow. We analyze a freely evolving idealized MITgcm front using horizontal coarse-graining and derive local budgets for resolved kinetic energy (KE) and eddy available potential energy (EAPE), retaining horizontal divergence, subfilter covariances, pressure-gradient work, vertical advection, and dissipation. The diagnosed flow exhibits a pronounced spatial asymmetry: convergent cyclonic cold filaments support forward KE and EAPE transfer, whereas divergent anticyclonic warm patches favor inverse transfer. Horizontal convergence and divergence also modulate other budget terms, including the isotropic cascade contributions, subfilter velocity–divergence and buoyancy–divergence couplings, and the local expansion or compression of resolved energy. These terms therefore inherit a cold–warm spatial organization from the cyclone–anticyclone pattern, while strain-dependent deviatoric transfer provides an additional pathway that can reinforce forward EAPE transfer under preferential cross-front compression. The results show that cyclone–anticyclone asymmetry spatially organizes both interscale cascades and other transfer terms in the local energy budgets.

SIGNIFICANCE STATEMENT: This study asks how mixed layer instability transfers energy across horizontal scales in physical space. By combining idealized MITgcm simulations with coarse-grained energy budgets, the work aims to connect cold-front sharpening, horizontal divergence, cyclonic preference, and local kinetic energy cascades.

1. Introduction

Mixed layer instability (MLI) is an ageostrophic form of baroclinic instability that draws on the available potential energy stored in lateral buoyancy gradients and restratifies the surface ocean. Early analyses of mixed-layer adjustment showed how horizontal density gradients can generate vertical stratification, while later stability studies distinguished baroclinic, symmetric, and gravitational modes in weakly stratified layers (Tandon and Garrett 1994, 1995; Haine and Marshall 1998). Nonlinear simulations then established that MLI grows near the mixed-layer deformation scale and produces mixed layer eddies (MLEs), whose overturning circulations slump fronts and reshape the vertical structure of the mixed layer (Boccaletti et al. 2007; Fox-Kemper et al. 2008; Fox-Kemper and Ferrari 2008; Callies et al. 2016). These results motivated parameterizations of MLE buoyancy fluxes for climate models, extending process-level theory to basin- and global-scale simulations (Fox-Kemper et al. 2011).

MLI is one of several interacting routes to submesoscale activity. Mesoscale strain can sharpen fronts and induce ageostrophic secondary circulations, while mixed-layer baroclinic, symmetric, and shear instabilities can amplify or fragment those fronts; idealized and regional studies document this transition and its energetic consequences (Capet et al. 2008a,b; Thomas and Ferrari 2008; Molemaker et al. 2005; McWilliams et al. 2009; Mahadevan and Tandon 2006; Nagai et al. 2006; Wang et al. 2021; Haney et al. 2015). The resulting currents are intermittent and spatially heterogeneous: frontogenesis, convergence, vertical motion, and vorticity are concentrated in filaments and eddy boundaries, rather than distributed uniformly across the mixed layer. This makes the local organization of their energy transfers a distinct question from the domain-mean energetics of a front.

Observations and realistic simulations show that submesoscale activity varies with season and background flow. Glider, mooring, and modeling studies find stronger mixed-layer submesoscales during winter, when deeper mixed layers favor MLI, while mesoscale strain and surface frontogen-

esis also contribute to regional variability (Mensa et al. 2013; Sasaki et al. 2014; Callies et al. 2015; Thompson et al. 2016; Buckingham et al. 2016; Yu et al. 2019; Whitt and Taylor 2017). These studies establish that MLI is dynamically important in both open-ocean and energetic-current settings, but also caution that its expression depends on stratification, forcing, and the interaction between mesoscale and submesoscale motions.

The consequences extend beyond restratification. Submesoscale fronts support vigorous vertical velocities and exchange between the mixed layer and thermocline; observed frontal turbulence and eddy-driven subduction demonstrate pathways for energy dissipation and tracer export, including particulate organic carbon (D'Asaro et al. 2011; Omand et al. 2015). Global simulations indicate that submesoscales contribute substantially to upper-ocean vertical heat transport, and recent process studies quantify MLI-driven exchange across the mixed-layer base (Su et al. 2018; Luo and Callies 2023). These processes are reviewed in broader accounts of submesoscale currents and their physical and biogeochemical impacts (McWilliams 2016; Mahadevan 2016). Submesoscale instabilities can also occur around mesoscale vortices, where their spatially asymmetric energy sources and sinks may affect eddy structure and subduction (Brannigan et al. 2017).

The scale-to-scale kinetic-energy (KE) transfer is itself bidirectional. Regional simulations have found forward transfer from fronts toward dissipative scales alongside upscale transfer as MLEs are absorbed by mesoscale eddies (Capet et al. 2008c; Schubert et al. 2020). In situ observations and localized energy budgets further show that the sign and magnitude of KE transfer depend on region, season, and flow structure; the same ocean can exhibit distinct forward and inverse pathways (Callies and Ferrari 2013; Naveira Garabato et al. 2022; Cao et al. 2021; Yang et al. 2021). Recent work links forward transfer to frontogenesis and convergent ageostrophic flow, while strain-related dynamics and eddy absorption can support upscale transfer (Srinivasan et al. 2023; Yu et al. 2024). Consequently, a domain- or time-averaged flux cannot identify which structures carry each pathway, nor determine whether a cascade term corresponds to local production or loss of resolved energy.

Horizontal coarse-graining provides a way to diagnose transfers simultaneously by scale and location, without relying on spatial homogeneity or isotropy (Aluie et al. 2018). Its application to MLI must, however, account for the fact that a near-surface horizontal flow is generally divergent even when the full three-dimensional velocity is incompressible. In particular, horizontal convergence is balanced by vertical variation in vertical velocity, and it is dynamically active in ageostrophic

frontal circulations. For a divergent horizontal flow, conservative flux-divergence and advective forms of the momentum and buoyancy tendencies are not interchangeable. Filtering them while suppressing divergence-related terms can therefore mix interscale transfer with direct expansion or compression of resolved energy and with subfilter correlations involving divergence. A local budget must retain these contributions if it is to distinguish cascade from transport, conversion, and resolved-flow compression.

This distinction is important for interpreting frontal energy transfers. In the horizontal KE budget, the subfilter-stress work can be separated into an isotropic component associated with compression and a deviatoric component associated with strain. The isotropic contribution is proportional to minus the resolved horizontal divergence times the trace of the subfilter velocity variance. It therefore favors forward transfer in convergent regions and inverse transfer in divergent regions, while the sign of the deviatoric contribution depends on the alignment of the subfilter stress with the resolved strain. Neither contribution is the same as the direct compression term in the resolved KE tendency, which depends on the resolved KE itself. A front may thus exhibit a forward cascade even as resolved energy is locally depleted by convergence, and the two effects need to be diagnosed separately.

The same need for separation arises in the EAPE budget. EAPE provides a scale-dependent measure of buoyancy anomalies, whereas its local tendency also reflects advection, vertical exchange, divergence-related coupling, and diffusion. For this reason, a forward EAPE cascade cannot by itself be interpreted as local EAPE production or destruction. Moreover, MITgcm records the temperature tendency in conservative flux form, while a coarse-grained decomposition of horizontal advection is naturally written in advective form. These horizontal partitions differ when horizontal divergence is nonzero, even though the complete three-dimensional advective tendency is consistent. We address this bookkeeping issue by defining an effective vertical-advection tendency as the residual needed to retain the native three-dimensional tendency while replacing its horizontal partition with the filtered advective decomposition. This permits a local EAPE budget to be evaluated without imposing horizontal nondivergence.

Here we apply this framework to an idealized, freely evolving frontal simulation with MITgcm. The 300-m water column has a vertically homogeneous upper 200 m and a stratified lower 100 m, allowing the model to represent both the weakly stratified mixed layer and the underlying thermo-

cline. We focus on the spatial organization of surface KE and EAPE transfers around developing cold cyclones, convergent filaments, and adjacent warm patches. In addition to the total fluxes, we diagnose the divergence-related and deviatoric contributions and distinguish them from direct resolved-energy tendencies, pressure work, and the vertical-advection contribution to EAPE.

The analysis addresses three linked questions. How are forward and inverse KE transfers distributed across the evolving frontal flow? How much of their local pattern is associated with isotropic compression, as opposed to rotation-invariant deviatoric deformation? And do the EAPE cascade and its divergence-related budget terms exhibit a corresponding organization in the same cold and warm structures? The diagnosed fields show forward KE and EAPE transfers in convergent cold filaments and inverse transfers in divergent warm patches. For KE, the sign of the isotropic contribution follows directly from the sign of horizontal divergence and the nonnegative subfilter velocity variance. For EAPE, the divergence contribution is proportional to minus horizontal divergence times the squared resolved buoyancy gradient, while cross-front compression can reinforce the forward cascade through the deviatoric term. The gradient-model interpretation also relates subfilter velocity–divergence and buoyancy–divergence covariances to gradients of the resolved fields. By treating these pathways together, the study clarifies how frontal compression helps organize interscale transfers during MLI and why those transfers must be interpreted separately from the local evolution of resolved energy.

2. Numerical Configuration and Dynamical Scaling

The initial buoyancy field follows the idealized frontal configuration used to study mixed layer instability and restratification (Boccaletti et al. 2007). A front centered at $y = y_0$ extends through the full 300 m water column. The upper $H_\mathrm{u} = 200$ m is vertically homogeneous. Below it, a constant vertical stratification with $N_0 = 20 f_0$ is superposed on the horizontal front, giving the initial buoyancy field

$$b(y,z) = \begin{cases} L_f B_y \tanh\left[(y-y_0)/L_f\right], & -H_\mathrm{u} \le z \le 0, \\ N_0^2 (z + H_\mathrm{u}) + L_f B_y \tanh\left[(y-y_0)/L_f\right], & -H_\mathrm{ML} \le z < -H_\mathrm{u}. \end{cases}$$

Here $L_f = 50$ km is the initial front width, $B_y = -0.5\times10^{-7}$ s^{-2} is the meridional buoyancy gradient at the frontal center, and $L_f B_y = -2.5\times10^{-3}$ m s^{-2} gives the signed far-field buoyancy amplitude. The lower branch is continuous at $z = -H_{\mathrm{u}}$. It retains the horizontal buoyancy gradient while adding the constant vertical gradient N_0^2; the 200–300 m layer therefore contains both horizontal and vertical temperature gradients.

The thermocline stratification is specified by $N_0/f_0 = 20$, which gives $N_0 = 1.46\times10^{-3}$ s^{-1} and $N_0^2 = 2.13\times10^{-6}$ s^{-2}. Using the full mixed-layer depth, the corresponding deformation radius is $L_{\mathrm{ML}} = N_0 H_{\mathrm{ML}}/f_0 = 6$ km. A small-amplitude perturbation that is white in the horizontal coordinates and uniform with depth is added to the initial buoyancy field, allowing unstable modes to develop without prescribing a preferred horizontal scale.

The freely decaying experiments are performed with the hydrostatic, three-dimensional Massachusetts Institute of Technology general circulation model (MITgcm; Marshall et al. 1997a; Marshall et al. 1997b) in an idealized reentrant channel. The domain is 200 km long in the along-front direction, 100 km wide in the cross-front direction, and $H = H_{\mathrm{ML}} = 300$ m deep. The upper $H_{\mathrm{u}} = 200$ m has no vertical stratification, whereas a prescribed thermocline occupies the lower 100 m. The uniform grid has $\Delta x = \Delta y = 250$ m, giving 800×400 horizontal cells, and $\Delta z = 5$ m, giving 60 vertical levels.

The simulations use an f plane with $f_0 = 7.29\times10^{-5}$ s^{-1} and zero planetary vorticity gradient. A rigid-lid formulation filters fast external gravity waves. The along-front direction is periodic, whereas the cross-front boundaries are closed, free-slip solid walls implemented by masking the northernmost and southernmost grid rows. This geometry allows disturbances to recirculate along the front while preventing cross-channel transport through the lateral boundaries.

Density is evaluated from a linear equation of state with temperature as the only active scalar. The thermal expansion coefficient is $\alpha_T = 2.0\times10^{-4}$ °C^{-1}, and gravitational acceleration is $g = 9.82$ m s^{-2}. Horizontal momentum dissipation is represented by biharmonic viscosity with $\nu_h = 10^6$ m^4 s^{-1}, and temperature uses biharmonic horizontal diffusivity $\kappa_{h,T} = 10^5$ m^4 s^{-1}. Vertical momentum and temperature mixing are harmonic, with $\nu_v = 10^{-4}$ m^2 s^{-1} and $\kappa_{v,T} = 10^{-5}$ m^2 s^{-1}, respectively.

Taking $U = 1$ m s^{-1} and $L_{\mathrm{ML}} = 6$ km, the horizontal dissipation ratios relative to the inertial-advection scale U^2/L_{ML} are $Re_h^{-1} = \nu_h/(UL_{\mathrm{ML}}^3) = 4.6\times10^{-6}$ and $Pe_h^{-1} = \kappa_{h,T}/(UL_{\mathrm{ML}}^3) =$

4.6×10^{-7}. Comparing the vertical harmonic terms with the same inertial scale gives $Re_z^{-1} = \nu_v L_{\mathrm{ML}}/(UH_{\mathrm{ML}}^2) = 6.7 \times 10^{-6}$ and $Pe_z^{-1} = \kappa_{v,T} L_{\mathrm{ML}}/(UH_{\mathrm{ML}}^2) = 6.7 \times 10^{-7}$. Thus, explicit viscosity and diffusion are weak at the deformation-radius scale, where baroclinic instability, frontal sharpening, and nonlinear advection control the leading-order dynamics. The biharmonic operators nevertheless remain important near the grid scale because their damping increases as k^4, preventing the accumulation of unresolved variance.

3. Flow evolution

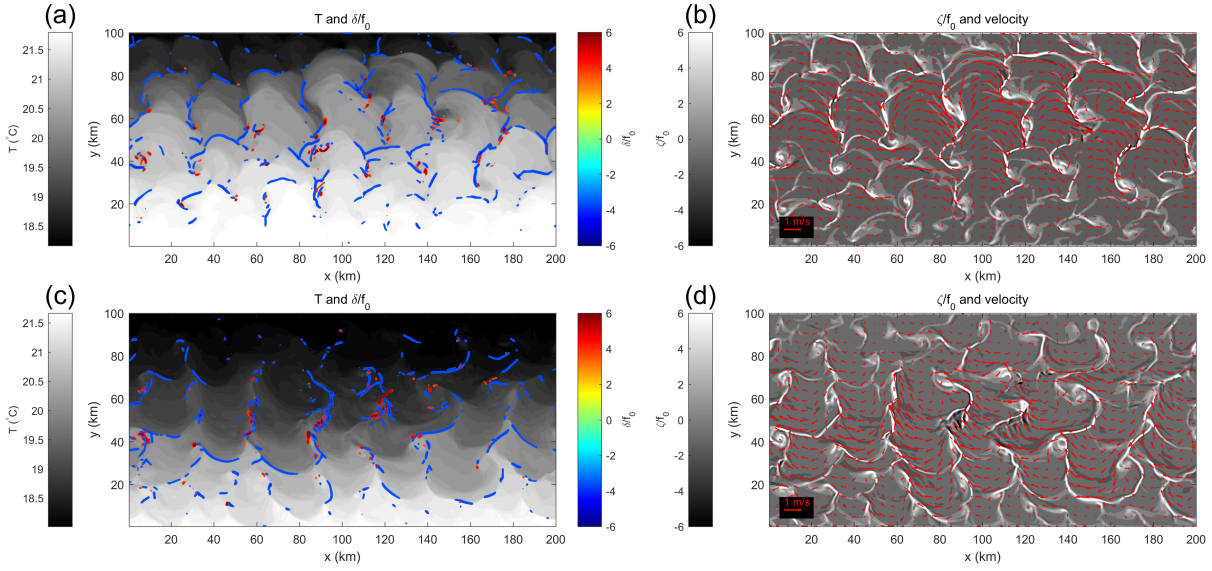


FIG. 1. Horizontal flow on day 9 at (a,b) the surface model level (2.5 m depth) and (c,d) near the mixed-layer base (295 m depth). In (a,c), grayscale shading shows temperature T (°C), and colored contours show normalized horizontal divergence δ/f_0, where $\delta = \partial_x u + \partial_y v$. Contours are drawn at $\delta/f_0 = \pm 3.6, \pm 4.2, \pm 4.8, \pm 5.4, \pm 6.0$. In (b,d), grayscale shading shows normalized vertical relative vorticity ζ/f_0, where $\zeta = \partial_x v - \partial_y u$, and red arrows represent the horizontal velocity (u, v); reference arrows indicate 1 m s^{-1}.

By day 9, MLI has transformed the initially zonal front into broad eddies separated by narrow filaments (figure 1). At the surface, frontal slumping lifts warm water from the southern side toward the surface, where it spreads northward and forms mesoscale anticyclonic warm eddies (figure 1(a,b)). Cold water from the northern side intrudes southward into the gaps between these eddies and is drawn into narrow, intense cold filaments. Convergence within the cold filaments is

much stronger than the divergence over the broad warm eddies. The vorticity and velocity fields in figure 1(b) show the corresponding concentration of cyclonic rotation along the filaments and in compact vortices, contrasting with the more diffuse anticyclonic circulation of the warm eddies.

Near the mixed-layer base, the flow exhibits a complementary structure with the thermal signatures reversed (figure 1(c,d)). Cold water originating north of the initial front descends and spreads southward, occupying much of the lower-level horizontal domain. These broad cold patches are associated with mesoscale anticyclonic circulation and relatively weak horizontal divergence. Strong convergence is concentrated in the narrow gaps between them, where warmer water intrudes northward as cyclonic filaments. The warm filaments near the base thus resemble the surface cold filaments in their narrow geometry, strong convergence, and cyclonic vorticity. The surface and lower-level flows share this contrast between broad anticyclonic eddies and narrow convergent cyclonic structures, despite their opposite temperature signatures.

The correspondence between the surface and lower-level structures during the early development of MLI motivates focusing the following energy-cascade and conversion analysis on the surface flow. Lower-level statistics are retained in figure 2 to illustrate this correspondence.

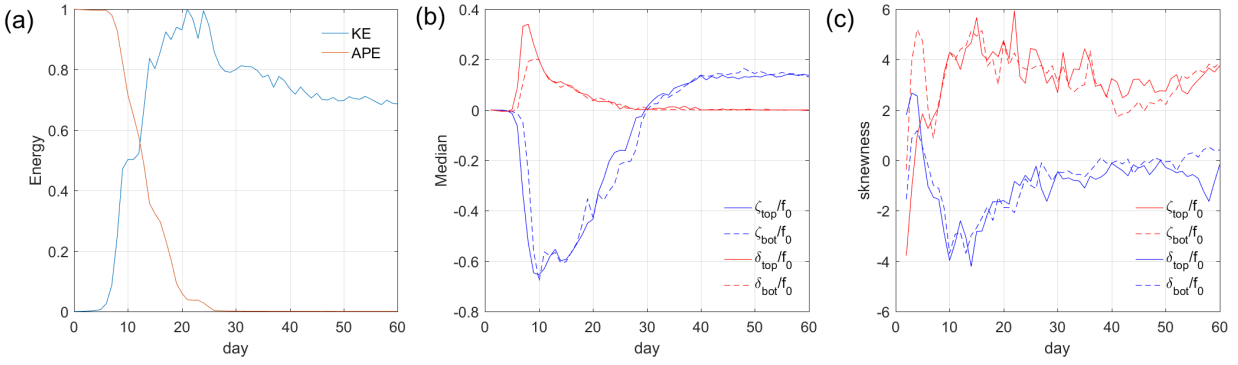


FIG. 2. Evolution of energy and velocity-gradient statistics during MLI. (a) Surface horizontal KE (blue) and quadratic eddy APE (orange), horizontally integrated and each normalized by its own maximum over the time series. (b) Horizontal medians of normalized relative vorticity ζ/f_0 (blue) and divergence δ/f_0 (red). (c) Horizontal skewness of ζ/f_0 (red) and δ/f_0 (blue). In (b,c), solid and dashed curves denote the top and bottom levels, respectively, at depths of 2.5 and 297.5 m.

The energy curves in figure 2(a) summarize the release of frontal APE during MLI. Horizontal KE is $K = (u^2 + v^2)/2$, the unfiltered counterpart of equation (1), and quadratic eddy APE is

$P = (g\alpha_T T')^2/(2N^2_{\mathrm{ref}})$, corresponding to the unfiltered limit of equations (10) and (11). During approximately days 10–30, the depletion of surface APE accompanies a rapid increase and subsequent peak in KE, consistent with MLI converting frontal APE into motion. After about day 30, APE remains small and KE evolves more slowly, with continued gradual decay. We therefore focus on the active adjustment period to diagnose the surface interscale transfers and the terms governing the KE and EAPE budgets.

The median statistics in figure 2(b) distinguish the spatially extensive background circulation from the intense filaments. During the early adjustment, positive divergence medians at both levels are consistent with the broad divergent warm patches at the surface and divergent cold patches near the base in figure 1. Coriolis deflection of the divergent flow favors anticyclonic circulation at both levels, giving negative vorticity medians. Around day 30, the vorticity medians change sign and remain positive through the end of the plotted 60-day interval. This shift is caused by the emergence of persistent surface cold cyclones and bottom warm cyclones. The positive medians indicate that cyclonic preference has extended from the intense-vorticity tail to the central part of the distribution.

Cyclonic asymmetry is already evident during the rapid adjustment at days 10–20, well before the vorticity medians become positive. In figure 2(c), positive vorticity skewness at both levels indicates an enhanced cyclonic tail, associated with the strong cold filaments at the surface and warm filaments at the bottom seen in figure 1. Thus, intense cyclonic structures coexist initially with a predominantly anticyclonic background. This organization is consistent with observed mixed-layer vorticity statistics (Shcherbina et al. 2013) and with cyclonic filaments and eddies in simulations of MLI and upper-ocean turbulence (Boccaletti et al. 2007; Roullet and Klein 2010). The simultaneous negative divergence skewness indicates a stronger convergent tail than divergent tail during this stage. This convergence–divergence asymmetry is another manifestation of the cyclone–anticyclone asymmetry. It is consistent with the frontogenetic feedback in which ageostrophic convergence accelerates gradient sharpening and intensifies frontal motions (Barkan et al. 2019; Srinivasan et al. 2023). The early coexistence of cyclonic and convergent tails motivates examining how these localized structures organize the energy transfers.

In the subsequent evolution, the surface cold filaments rapidly roll up and merge into compact cold cyclones that can remain coherent for several months. Their longevity permits repeated eddy

interactions well beyond the initial growth phase of MLI. This evolution is consistent with numerical evidence that MLI feeds an inverse KE cascade (Callies et al. 2016) and that absorption of mixed layer eddies by mesoscale eddies transfers KE upscale over several months (Schubert et al. 2020). Observations provide complementary, indirect evidence: seasonal KE maxima at scales below 60 km precede those at 60–300 km by 1–4 months, consistent with an upscale progression of energy supplied by mixed layer instability (Steinberg et al. 2022). These results motivate distinguishing the intense convergence within filaments from the longer-term eddy interactions associated with upscale energy transfer.

4. Coarse-Grained Energy Framework

We use horizontal coarse-graining to diagnose the local redistribution of kinetic and eddy available potential energy across scales. This framework explicitly reveals how horizontal divergence affects the different contributions to the energy budgets of the resolved (low-pass-filtered) flow near the surface.

a. Coarse-grained horizontal kinetic-energy budget near the surface

We first derive the budget for the resolved horizontal kinetic energy,

$$K^\ell = \frac{1}{2}(u_i^\ell)^2 \tag{1}$$

obtained by filtering the horizontal velocity at scale ℓ. Here, the subscript denotes the horizontal direction, with $u_1 = u$ and $u_2 = v$, and repeated indices are summed. The superscript ℓ denotes convolution with the Gaussian low-pass kernel

$$G_\ell(r) = \frac{9}{2\pi\ell^2}\exp\left(-\frac{9r^2}{2\ell^2}\right), \tag{2}$$

where r is the horizontal distance from the kernel center. The filter attenuates fluctuations at scales smaller than ℓ. For the near-surface horizontal momentum budget, we neglect vertical advection while retaining horizontal divergence and viscous effects. Under this approximation, the horizontal

momentum equation becomes

$$\partial_t u_i + u_j \partial_j u_i + f_0 \epsilon_{i3j} u_j = -\partial_i \phi + \mathcal{D}_i,$$

with $\mathcal{D}_i = -\nu_h \nabla_h^4 u_i + \nu_v \partial_{zz} u_i$ representing the momentum dissipation. Although the three-dimensional flow is incompressible, its horizontal component is generally divergent near the surface:

$$\delta = \partial_j u_j = \partial_x u + \partial_y v \neq 0.$$

Using $u_j \partial_j u_i = \partial_j (u_i u_j) - u_i \delta$, we rewrite the momentum equation as

$$\partial_t u_i + \partial_j (u_i u_j) - u_i \delta + f_0 \epsilon_{i3j} u_j = -\partial_i \phi + \mathcal{D}_i.$$

Low-pass filtering this equation gives

$$\partial_t u_i^\ell + u_j^\ell \partial_j u_i^\ell + \partial_j \tau_{ij}^\ell - \tau_\ell(u_i, \delta) + f_0 \epsilon_{i3j} u_j^\ell = -\partial_i \phi^\ell + \mathcal{D}_i^\ell. \tag{3}$$

Here the subfilter stress and velocity–divergence covariance are defined by

$$\tau_{ij}^\ell(\boldsymbol{u}, \boldsymbol{u}) = (u_i u_j)^\ell - u_i^\ell u_j^\ell,$$
$$\tau_\ell(u_i, \delta) = (u_i \delta)^\ell - u_i^\ell \delta^\ell.$$

Multiplying equation (3) by u_i^ℓ and using the identities

$$u_i^\ell \partial_t u_i^\ell = \partial_t K^\ell,$$
$$u_i^\ell u_j^\ell \partial_j u_i^\ell = \partial_j (u_j^\ell K^\ell) - \delta^\ell K^\ell,$$
$$u_i^\ell \partial_j \tau_{ij}^\ell = \partial_j (u_i^\ell \tau_{ij}^\ell) - \tau_{ij}^\ell \partial_j u_i^\ell.$$

yields the local coarse-grained kinetic-energy budget

$$\partial_t K^\ell + \nabla_h \cdot \left[\boldsymbol{u}^\ell K^\ell + u_i^\ell \tau_{ij}^\ell \right] = -\Pi_K^\ell - A_K^\ell - C_K^\ell + \Pi_a^\ell + \mathcal{D}_K^\ell. \tag{4}$$

Let $\langle\cdot\rangle_h$ denote a horizontal average. Under the stated periodic and free-slip boundary treatment, the averaged flux divergence on the left of equation (4) vanishes. Thus,

$$\partial_t \langle K^\ell \rangle_h = -\langle \Pi_K^\ell \rangle_h - \langle A_K^\ell \rangle_h - \langle C_K^\ell \rangle_h + \langle \Pi_a^\ell \rangle_h + \langle \mathcal{D}_K^\ell \rangle_h. \tag{5}$$

We next examine the physical interpretation and spatial distribution of each term in the coarse-grained kinetic-energy budget in equation (4).

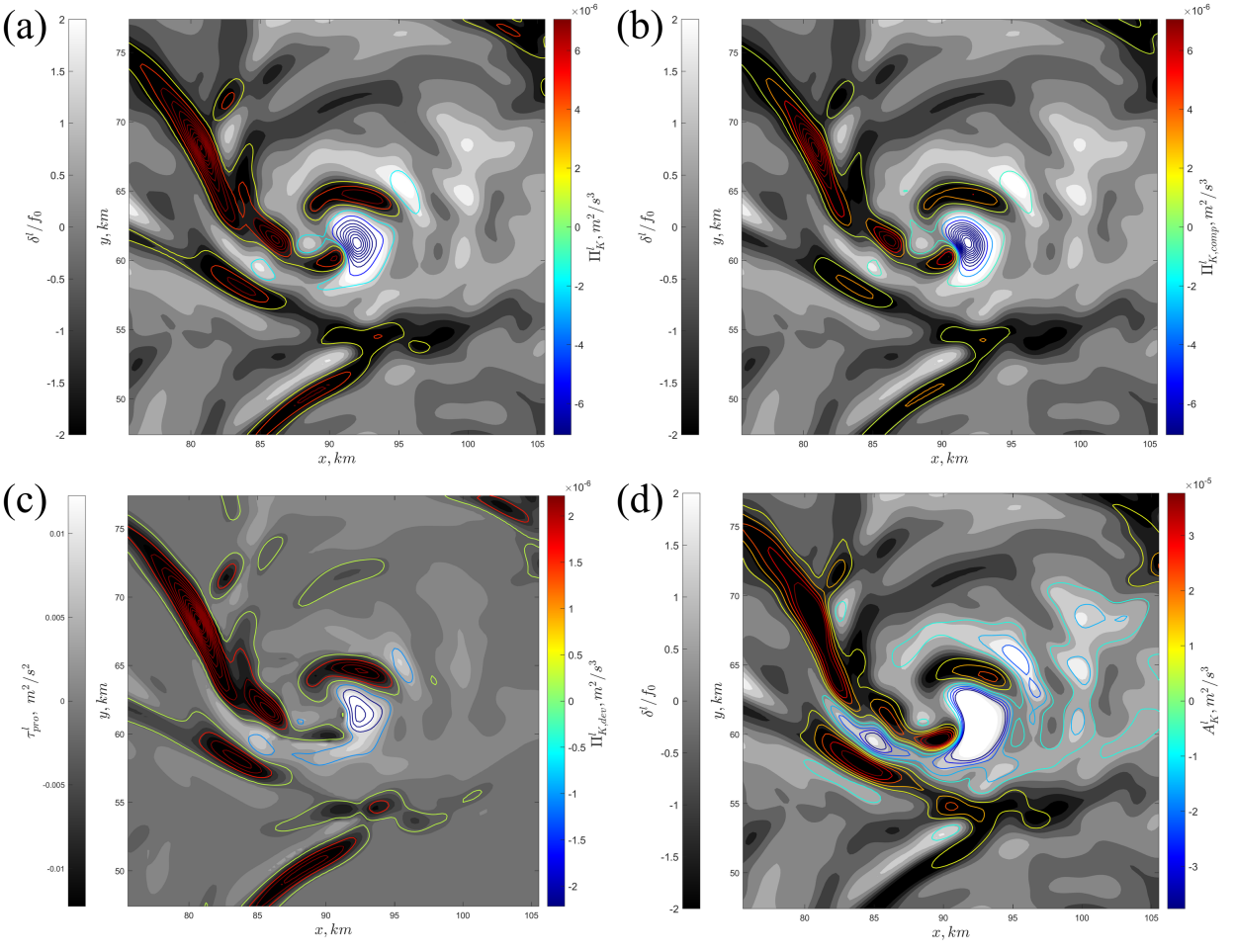


FIG. 3. Spatial distributions of the resolved and subfilter kinetic-energy terms at $\ell = 5\,\mathrm{km}$ on day 10. The grayscale background in panels (a, b, d) denotes the normalized horizontal divergence δ^ℓ/f_0 while that in (c) represents the projected deviatoric subfilter stress $\tau^\ell_{\mathrm{proj}}$ in equation (6). Colored contours in panels (a–d) show the total kinetic energy cascade Π^ℓ_K, its compressive contribution $\Pi^\ell_{K,\mathrm{comp}}$, deviatoric contribution $\Pi^\ell_{K,\mathrm{dev}}$, and the expansion/compression of K^ℓ due to A^ℓ_K, respectively.

The first term on the right-hand side,

$$\Pi_K^\ell = -\tau_{ij}^\ell S_{ij}^\ell = -\tau_{11}^\ell \partial_x u^\ell - \tau_{22}^\ell \partial_y v^\ell - \tau_{12}^\ell \left(\partial_y u^\ell + \partial_x v^\ell \right)$$

is the deformation work associated with the subfilter stress τ_{ij} and the resolved strain $S_{ij}^\ell = \frac{1}{2}(\partial_j u_i^\ell + \partial_i u_j^\ell)$. A positive Π_K^ℓ denotes a forward kinetic-energy cascade from scales larger than ℓ to smaller scales through deformation work; a negative value denotes an upscale cascade. Previous studies have linked frontal convergence and frontogenesis to enhanced forward kinetic-energy cascade and identified distinct convergence- and strain-related contributions to the cascade (Srinivasan et al. 2023; Yu et al. 2024). Consistent with these earlier findings, figure 3(a) reveals a clear spatial correspondence between the horizontal convergence and the total kinetic-energy transfer in the freely decaying MLI surface flow. During the early formation of cold vortices, regions of convergence ($\delta^\ell < 0$) coincide with $\Pi_K^\ell > 0$ (forward transfer), while regions of divergence coincide with $\Pi_K^\ell < 0$ (upscale transfer). To determine how horizontal convergence contributes to the observed cascade pattern, we decompose Π_K^ℓ into contributions associated with isotropic compression, normal strain $\sigma^\ell = \partial_x u^\ell - \partial_y v^\ell$, and shear strain $\gamma^\ell = \partial_y u^\ell + \partial_x v^\ell$ as

$$\Pi_K^\ell = \Pi_{K,\mathrm{comp}}^\ell + \Pi_{K,\mathrm{normal}}^\ell + \Pi_{K,\mathrm{shear}}^\ell.$$

The isotropic compression contribution is

$$\Pi_{K,\mathrm{comp}}^\ell = -\frac{\delta^\ell}{2}(\tau_{11}^\ell + \tau_{22}^\ell).$$

Because the subfilter velocity variance $\tau_{11}^\ell + \tau_{22}^\ell = (|\boldsymbol{u}|^2)^\ell - |\boldsymbol{u}^\ell|^2$ is nonnegative, $\Pi_{K,\mathrm{comp}}^\ell$ is positive in convergent regions and negative in divergent regions, as illustrated in figure 3(b). The comparable magnitudes of Π_K^ℓ and $\Pi_{K,\mathrm{comp}}^\ell$ in panels (a) and (b) indicate that isotropic compression contributes substantially to the total transfer pattern. Differences between the panels reflect the additional normal- and shear-strain contributions.

The normal strain σ^ℓ describes deviatoric deformation: extension along one horizontal coordinate axis accompanied by compression along the other. Its cascade contribution is

$$\Pi^\ell_{K,\mathrm{normal}} = -\frac{\sigma^\ell}{2}(\tau^\ell_{11} - \tau^\ell_{22}),$$

where $\tau^\ell_{11} - \tau^\ell_{22}$ measures the anisotropy of the subfilter velocity variance. This term is positive when that variance is larger along the compressive direction. For example, cross-front contraction combined with along-front extension can lead to $\Pi^\ell_{K,\mathrm{normal}} > 0$ and transfer kinetic energy downscale.

The shear-strain contribution

$$\Pi^\ell_{K,\mathrm{shear}} = -\gamma^\ell \tau^\ell_{12}$$

is positive when $\gamma^\ell \tau^\ell_{12} < 0$, meaning that the subfilter stress opposes the resolved shear. This mechanism is analogous to Reynolds-stress production in turbulent shear flows and is expected to be particularly relevant along frontal jets, vortex edges, and strongly sheared filaments.

The normal- and shear-strain contributions depend individually on the orientation of the coordinate axes. Their sum defines the rotation-invariant deviatoric transfer:

$$\Pi^\ell_{K,\mathrm{dev}} = \Pi^\ell_{K,\mathrm{normal}} + \Pi^\ell_{K,\mathrm{shear}} = -\sqrt{(\sigma^\ell)^2 + (\gamma^\ell)^2}\,\tau^\ell_{\mathrm{proj}}$$

Here,

$$\tau^\ell_{\mathrm{proj}} \equiv \frac{1}{2}(\tau^\ell_{11} - \tau^\ell_{22})\cos 2\alpha + \tau^\ell_{12}\sin 2\alpha \tag{6}$$

measures the anisotropy of the subfilter stress in the principal-strain frame. The relative orientation of the principal-strain axes and the buoyancy-front directions is illustrated in figure 4. α denotes the angle between the extensional principal-strain axis and the x axis, and it is determined by

$$\cos 2\alpha = \frac{\sigma^\ell}{\sqrt{(\sigma^\ell)^2 + (\gamma^\ell)^2}}, \qquad \sin 2\alpha = \frac{\gamma^\ell}{\sqrt{(\sigma^\ell)^2 + (\gamma^\ell)^2}}.$$

If $\tau^\ell_{\mathrm{proj}} < 0$, the variance is larger along the compressive axis and $\Pi^\ell_{K,\mathrm{dev}} > 0$, indicating forward cascade. This pattern is evident along the contracting filaments in figure 3(c).

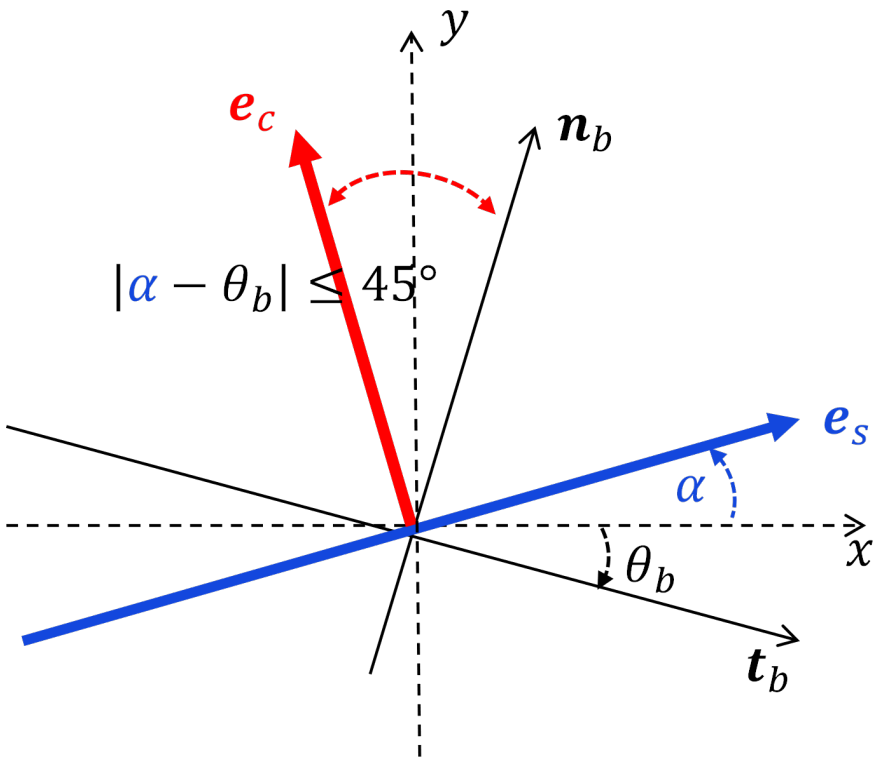


FIG. 4. Geometry relating the principal-strain frame to a buoyancy front. The extensional and compressional axes are $\boldsymbol{e}_s$ (blue) and $\boldsymbol{e}_c$ (red), respectively, with α denoting the angle of $\boldsymbol{e}_s$ relative to the x axis. The across-front and along-front directions are $\boldsymbol{n}_b$ and $\boldsymbol{t}_b$, respectively, and θ_b is the angle of $\boldsymbol{t}_b$ relative to the x axis. The condition $|\alpha - \theta_b| < 45°$ places the along-front direction within 45° of the extensional principal-strain axis such that the deviatoric strain drives a forward potential-energy cascade according to equation (24).

Unlike the interscale transfer Π_K^ℓ, the term

$$A_K^\ell = -\delta^\ell K^\ell = -\nabla_h \cdot (\boldsymbol{u}^\ell K^\ell) + \boldsymbol{u}^\ell \cdot \nabla_h K^\ell$$

represents the local contribution of resolved horizontal expansion or compression to the kinetic-energy budget. Since $K^\ell \geq 0$, A_K^ℓ has the opposite sign to δ^ℓ, as illustrated in figure 3(d). In a convergent cold filament, $-A_K^\ell = \delta^\ell K^\ell < 0$, so this term contributes negatively to the local budget of K^ℓ. The magnitude of A_K^ℓ can be several times larger than that of Π_K^ℓ.

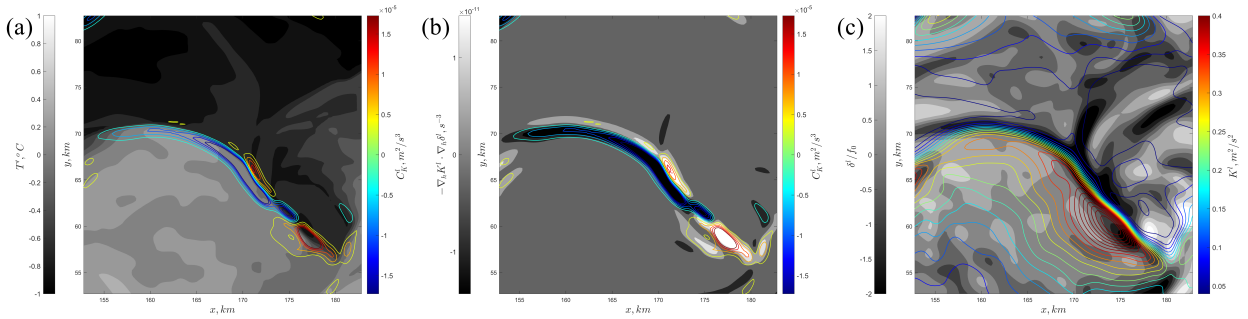


FIG. 5. Fine structure of a cold filament along the edge of a warm anticyclonic eddy at $\ell = 5\,\mathrm{km}$ on day 10. Colored contours in (a) and (b) show C_K^ℓ ($\mathrm{m^2\,s^{-3}}$); their grayscale backgrounds show (a) the surface temperature anomaly T' (°C) and (b) the Clark-model predictor $-\nabla_h K^\ell \cdot \nabla_h \delta^\ell$ defined in equation (8). In (c), colored contours show resolved kinetic energy K^ℓ and the grayscale background shows normalized horizontal divergence δ^ℓ / f_0.

The third term on the right-hand side of equation (4)

$$C_K^\ell = -u_i^\ell \tau_\ell(u_i, \delta) \tag{7}$$

represents the coupling of the resolved velocity with the subfilter velocity–divergence covariance. The covariance can be approximated as

$$\tau_\ell(u_i, \delta) \equiv (u_i \delta)^\ell - u_i^\ell \delta^\ell \simeq C_G \ell^2\, \partial_k u_i^\ell\, \partial_k \delta^\ell,$$

using the gradient model of Clark et al. (1979), derived in appendix A. The positive coefficient C_G is set by the second moment of the Gaussian kernel in equation (2). Substituting this approximation into equation (7) gives

$$C_K^\ell \simeq -C_G \ell^2 u_i^\ell \partial_k u_i^\ell\, \partial_k \delta^\ell = -C_G \ell^2 \nabla_h K^\ell \cdot \nabla_h \delta^\ell. \tag{8}$$

Figure 5(a) shows a cold cyclonic filament wrapping around the edge of a warm anticyclonic eddy. Across most of the filament, the gradients of K^ℓ and δ^ℓ are aligned (figure 5(c)). Equation (8) therefore predicts $C_K^\ell < 0$ in the filament, which contributes positively to the local K^ℓ budget. Panel (b) compares the directly computed C_K^ℓ with its gradient-model predictor, $-\nabla_h K^\ell \cdot \nabla_h \delta^\ell$; their spatial correspondence supports this interpretation.

The fourth term on the right-hand side of equation (4),

$$\Pi_a^\ell = -u_i^\ell \partial_i \phi^\ell = f_0 \boldsymbol{k} \cdot (\boldsymbol{u}_g^\ell \times \boldsymbol{u}_a^\ell),$$

is the work done by the resolved horizontal pressure-gradient force $-\nabla_h \phi^\ell$ on $\boldsymbol{u}^\ell$. The second equality follows from geostrophic balance,

$$f_0 \boldsymbol{k} \times \boldsymbol{u}_g^\ell = -\nabla_h \phi^\ell,$$

where $\boldsymbol{k}$ is the vertical unit vector and $\boldsymbol{u}_a^\ell = \boldsymbol{u}^\ell - \boldsymbol{u}_g^\ell$ is the ageostrophic component of the resolved flow. Positive Π_a^ℓ indicates that the resolved horizontal pressure-gradient force supplies kinetic energy, whereas negative Π_a^ℓ indicates its removal. These signs correspond to ageostrophic motion down and up the pressure-potential gradient, respectively. Figure 6(a) shows both signs at the periphery of a newborn cyclone with a low-pressure center: outward and inward $\boldsymbol{u}_a^\ell$ are associated with negative and positive Π_a^ℓ, respectively.

To relate pressure-gradient work to vortex dynamics, consider an approximately axisymmetric cold cyclone. Let r increase outward, and take $u_\theta > 0$ to denote counterclockwise rotation. The gradient-wind balance gives

$$u_{g,\theta} = \frac{1}{f_0} \partial_r \phi = u_\theta + \frac{u_\theta^2}{f_0 R}.$$

Here R is the curvature radius. The azimuthal ageostrophic velocity is therefore

$$u_{a,\theta} = u_\theta - u_{g,\theta} = -\frac{u_\theta^2}{f_0 R} < 0.$$

When cold filaments spiral into a cyclone, R decreases, increasing $|u_{a,\theta}|$. The negative azimuthal ageostrophic velocity in figure 6(b) is consistent with this balance, but its sign does not determine the radial flow. The connection between radial inflow and cyclonic spin-up follows from the tangential momentum equation

$$\partial_t u_\theta + u_r(\zeta + f_0) = 0, \qquad \zeta = \frac{1}{r} \partial_r (r u_\theta).$$

Therefore, cyclonic spin-up ($\partial_t u_\theta > 0$) corresponds to an inward ageostrophic flow

$$u_{a,r} = u_r = -\frac{\partial_t u_\theta}{f_0 + \zeta} < 0, \tag{9}$$

provided $u_{g,r} = 0$ due to the axisymmetric pressure field ϕ and $f_0 + \zeta > 0$ in cyclones. Since the pressure potential increases away from the low-pressure core ($\partial_r \phi^\ell > 0$), the inward ageostrophic flow ($u^\ell_{a,r} < 0$) moves down the pressure gradient and gives $\Pi^\ell_a \simeq -u^\ell_{a,r} \partial_r \phi^\ell > 0$. Conversely, a local outward flow ($u^\ell_{a,r} > 0$) moves up that gradient, decelerates u_θ, and gives $\Pi^\ell_a < 0$. Under equation (9), the positive and negative patches in figure 6(a) are thus consistent with inflow and outflow near the forming cyclone.

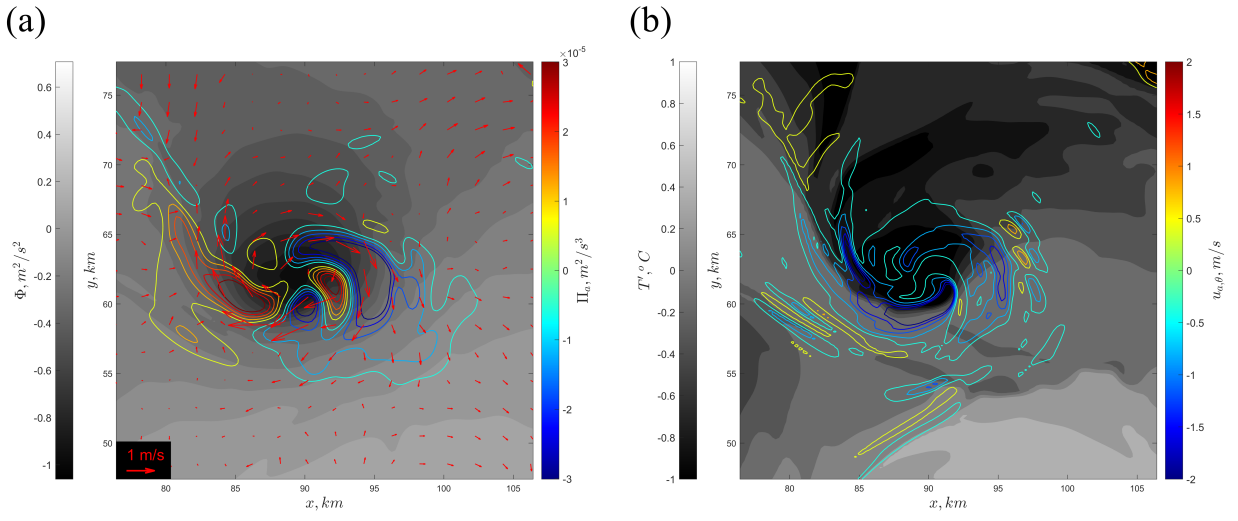


FIG. 6. (a) Filtered ageostrophic flow $\boldsymbol{u}^\ell_a$ (red arrows), pressure potential ϕ (grayscale background), and horizontal pressure-gradient work Π^ℓ_a (colored contours) near a newborn cyclone at $\ell = 5$ km on day 10. (b) Grayscale shows the temperature perturbation T' and colored contours show the azimuthal ageostrophic velocity $u_{a,\theta}$.

The final term in equation (4), $\mathcal{D}^\ell_K = -\nu_h u^\ell_i \nabla^4_h u^\ell_i + \nu_v u^\ell_i \partial_{zz} u^\ell_i$, is the local viscous contribution. Its magnitude is usually an order of magnitude smaller than the other terms over most scales of interest; its spatial distribution is not shown here.

b. Coarse-grained eddy available potential-energy budget

To complement the kinetic-energy budget, we derive the coarse-grained eddy available potential-energy budget from the three-dimensional temperature equation. Unlike the approximate horizontal

momentum budget above, this budget retains vertical advection. At a fixed vertical level, temperature evolves according to

$$\partial_t T = -\boldsymbol{u}_h \cdot \nabla_h T - w\,\partial_z T + D_T,$$

where $\boldsymbol{u}_h = (u, v)$ and w is positive upward. The diffusion tendency $D_T = -\kappa_{4,T}\nabla_h^4 T + \kappa_{v,T}\,\partial_{zz} T$ combines biharmonic lateral diffusion with $\kappa_{4,T} = 10^5\ \mathrm{m^4\,s^{-1}}$ and harmonic vertical diffusion with $\kappa_{v,T} = 10^{-5}\ \mathrm{m^2\,s^{-1}}$, the values used in this MITgcm experiment. We define the temperature anomaly relative to the horizontal mean and the corresponding normalized buoyancy anomaly as

$$T' = T - \langle T \rangle_h, \qquad \beta = \frac{\alpha_T g}{N_{\mathrm{ref}}}, \qquad b = \beta T', \tag{10}$$

where a prime denotes departure from the horizontal mean, so that $\langle T' \rangle_h = \langle b \rangle_h = 0$. Here α_T is the thermal expansion coefficient, $g = 9.82\ \mathrm{m\,s^{-2}}$ is the gravitational acceleration, $N_{\mathrm{ref}} = 5 f_0$ is the reference mixed-layer buoyancy frequency, and $f_0 = 7.29 \times 10^{-5}\ \mathrm{s^{-1}}$ is the Coriolis parameter. The normalized anomaly b has units of velocity.

The resolved low-pass quadratic eddy APE at horizontal filter scale ℓ is

$$P^\ell = \frac{1}{2}(b^\ell)^2 = \frac{1}{2N_{\mathrm{ref}}^2}\left[(g\alpha_T T')^\ell\right]^2. \tag{11}$$

Below, we derive the native closure equation for P^ℓ by writing the temperature equation in conservative flux form,

$$\partial_t T = H_T + V_T + D_T, \tag{12}$$

with the horizontal and vertical flux-divergence tendencies

$$H_T = -\nabla_h \cdot (\boldsymbol{u}_h T), \qquad V_T = -\partial_z (wT). \tag{13}$$

This conservative form preserves the flux-divergence structure and the associated boundary conditions. For an incompressible continuous velocity field, $H_T + V_T = -\boldsymbol{u}_h \cdot \nabla_h T - wT_z$. Subtracting the horizontal mean of equation (12) and using equation (10) gives

$$\partial_t b = H_b' + V_b' + D_b',$$

where $H'_b = \beta H'_T$, $V'_b = \beta V'_T$, and $D'_b = \beta D'_T$. Filtering the above equation and then multiplying by b^ℓ gives the native closure for P^ℓ:

$$\partial_t P^\ell = b^\ell (H'_b)^\ell + b^\ell (V'_b)^\ell + b^\ell (D'_b)^\ell \tag{14}$$

To expose the potential energy cascade across the filter scale ℓ, the horizontal buoyancy advection $\mathcal{H}_{b,\mathrm{adv}} = -\boldsymbol{u}_h \cdot \nabla_h b$ is filtered to give

$$(\mathcal{H}_{b,\mathrm{adv}})^\ell = -\nabla_h \cdot (\boldsymbol{u}_h b)^\ell + (b\delta)^\ell = -\nabla_h \cdot \left[\boldsymbol{u}_h^\ell b^\ell + \boldsymbol{\tau}^\ell(\boldsymbol{u}_h, b)\right] + (b\delta)^\ell, \tag{15}$$

where $\boldsymbol{\tau}^\ell(\boldsymbol{u}_h, b) = (\boldsymbol{u}_h b)^\ell - \boldsymbol{u}_h^\ell b^\ell$ is the subfilter horizontal buoyancy flux. After multiplication by b^ℓ, the two divergence terms on the right-hand side expand as

$$b^\ell \nabla_h \cdot (\boldsymbol{u}_h^\ell b^\ell) = \nabla_h \cdot (\boldsymbol{u}_h^\ell P^\ell) + P^\ell \delta^\ell, \tag{16}$$

$$b^\ell \nabla_h \cdot \boldsymbol{\tau}^\ell(\boldsymbol{u}_h, b) = \nabla_h \cdot \left[b^\ell \boldsymbol{\tau}^\ell(\boldsymbol{u}_h, b)\right] - \boldsymbol{\tau}^\ell(\boldsymbol{u}_h, b) \cdot \nabla_h b^\ell, \tag{17}$$

with $\tau^\ell(b, \delta) = (b\delta)^\ell - b^\ell \delta^\ell$ representing the subfilter buoyancy–divergence covariance. Collecting the terms in equations (15) to (17) gives

$$b^\ell (\mathcal{H}_{b,\mathrm{adv}})^\ell = -\nabla_h \cdot \boldsymbol{F}_P^\ell - \Pi_P^\ell - A_P^\ell - C_P^\ell. \tag{18}$$

Here, $\boldsymbol{F}_P^\ell = \boldsymbol{u}_h^\ell P^\ell + b^\ell \boldsymbol{\tau}^\ell(\boldsymbol{u}_h, b)$ is the horizontal transport flux of P^ℓ. Its divergence has zero horizontal mean, $\left\langle \nabla_h \cdot \boldsymbol{F}_P^\ell \right\rangle_h = 0$, under the periodic and zero-normal-flux boundary conditions.

The nonlinear cascade of P^ℓ across ℓ is

$$\Pi_P^\ell = -\nabla_h b^\ell \cdot \boldsymbol{\tau}^\ell(\boldsymbol{u}_h, b) \tag{19}$$

with positive and negative values denoting forward (downscale) and inverse (upscale) cascades, respectively. Figure 7(a) shows the spatial pattern of Π_P^ℓ near a newborn cyclone. Convergent cold filaments spiral inward and exhibit a forward cascade ($\Pi_P^\ell > 0$), whereas divergent warm patches ($\delta^\ell > 0$) exhibit an inverse cascade ($\Pi_P^\ell < 0$).

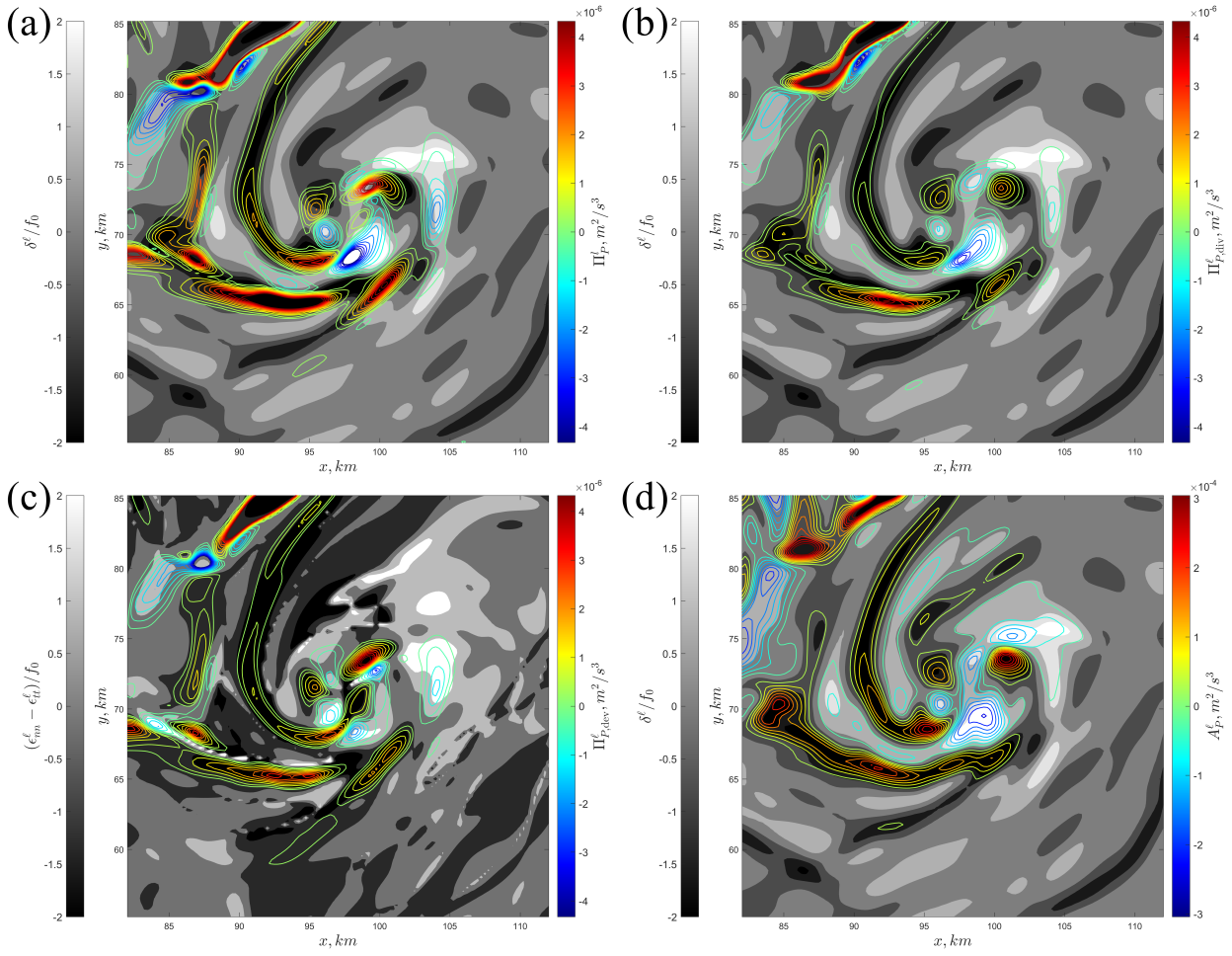


FIG. 7. Potential energy cascades and the divergence-related contribution to the P^ℓ budget near a newborn cyclone at $\ell = 4$km on day 11. The colored contours denote Π^ℓ_P in panel (a), $\Pi^\ell_{P,\mathrm{div}}$ in (b), $\Pi^\ell_{P,\mathrm{dev}}$ in (c), and A^ℓ_P in (d). The grayscale in panels (a), (b), and (d) denotes the filtered divergence δ^ℓ, whereas that in (c) denotes $(\epsilon^\ell_{nn} - \epsilon^\ell_{tt})$ on the right-hand side of equation (24); both are normalized by f_0.

To interpret this spatial correspondence, we approximate the subfilter buoyancy flux $\boldsymbol{\tau}^\ell(\boldsymbol{u}_h, b)$ using the gradient-model approximation:

$$\tau^\ell(u_i, b) \simeq C_G \ell^2 (\partial_j u_i^\ell)(\partial_j b^\ell).$$

Equation (19) then becomes

$$\Pi^\ell_P \simeq -C_G \ell^2 (\nabla_h b^\ell)^\mathsf{T} \boldsymbol{S}^\ell \nabla_h b^\ell,$$

where $\boldsymbol{S}^\ell = [\nabla_h \boldsymbol{u}_h^\ell + (\nabla_h \boldsymbol{u}_h^\ell)^\mathsf{T}]/2$ is the horizontal strain tensor for the resolved flow $\boldsymbol{u}_h^\ell$. In two dimensions, the strain tensor separates into its isotropic part $\delta^\ell \boldsymbol{I}/2$ and deviatoric part $\boldsymbol{S}^\ell_{\mathrm{dev}} = \boldsymbol{S}^\ell - \delta^\ell \boldsymbol{I}/2$. Therefore Π_P^ℓ decomposes into

$$\Pi_P^\ell \simeq \Pi_{P,\mathrm{div}}^\ell + \Pi_{P,\mathrm{dev}}^\ell, \tag{20}$$

with

$$\Pi_{P,\mathrm{div}}^\ell = -\frac{C_G \ell^2}{2} \delta^\ell |\nabla_h b^\ell|^2, \tag{21}$$

$$\Pi_{P,\mathrm{dev}}^\ell = -C_G \ell^2 (\nabla_h b^\ell)^\mathsf{T} \boldsymbol{S}^\ell_{\mathrm{dev}} \nabla_h b^\ell, \tag{22}$$

shown in figure 7(b) and (c), respectively. For a nonzero buoyancy gradient, equation (21) predicts a forward isotropic cascade in convergent regions ($\delta^\ell < 0$) and an inverse cascade in divergent regions ($\delta^\ell > 0$; figure 7(b)). The comparable magnitudes of Π_P^ℓ in panel (a) and $\Pi_{P,\mathrm{div}}^\ell$ in panel (b) suggest that the isotropic cascade accounts for a substantial part of the total cascade in the convergent cold filaments. In contrast, the sign of $\Pi_{P,\mathrm{dev}}^\ell$ in equation (22) depends on the orientation of $\nabla_h b^\ell$ relative to the principal-strain axes (figure 4). Define orthogonal unit vectors normal and tangent to the local buoyancy front by

$$\boldsymbol{n}_b = \frac{\nabla_h b^\ell}{|\nabla_h b^\ell|}, \qquad \boldsymbol{t}_b \cdot \boldsymbol{n}_b = 0. \tag{23}$$

The cross-front and along-front normal strain rates are then

$$\epsilon_{nn}^\ell = \boldsymbol{n}_b^\mathsf{T} \boldsymbol{S}^\ell \boldsymbol{n}_b, \qquad \epsilon_{tt}^\ell = \boldsymbol{t}_b^\mathsf{T} \boldsymbol{S}^\ell \boldsymbol{t}_b.$$

Their sum gives the horizontal divergence $\delta^\ell = \epsilon_{nn}^\ell + \epsilon_{tt}^\ell$, whereas their difference follows from the deviatoric projection,

$$\boldsymbol{n}_b^\mathsf{T} \boldsymbol{S}^\ell_{\mathrm{dev}} \boldsymbol{n}_b = (\epsilon_{nn}^\ell - \epsilon_{tt}^\ell)/2.$$

Consequently, equation (22) becomes

$$\Pi_{P,\mathrm{dev}}^\ell = -\frac{C_G \ell^2}{2} (\epsilon_{nn}^\ell - \epsilon_{tt}^\ell) |\nabla_h b^\ell|^2. \tag{24}$$

Geometrically, when the along-front direction lies within 45° of the principal extensional axis $\boldsymbol{e}_s$, $|\alpha - \theta_b| < 45°$ in figure 4 implies that the along-front normal strain rate exceeds the cross-front normal strain rate, $\epsilon^\ell_{tt} > \epsilon^\ell_{nn}$. For convergent filaments with $\delta^\ell = \epsilon^\ell_{nn} + \epsilon^\ell_{tt} < 0$, equations (20), (21) and (24) then imply

$$\Pi^\ell_{P,\mathrm{div}} > 0, \qquad \Pi^\ell_{P,\mathrm{dev}} > 0, \qquad \Pi^\ell_P > 0,$$

Thus, both the isotropic and deviatoric contributions support a forward potential-energy cascade.

In addition to the interscale cascade Π^ℓ_P, the resolved horizontal divergence δ^ℓ enters the P^ℓ budget in equation (18) through

$$A^\ell_P = -\delta^\ell P^\ell.$$

This term represents resolved horizontal expansion or compression in the P^ℓ budget. For $P^\ell > 0$, it has the opposite sign to δ^ℓ and enters the budget with a minus sign. Its spatial distribution is shown in figure 7(d).

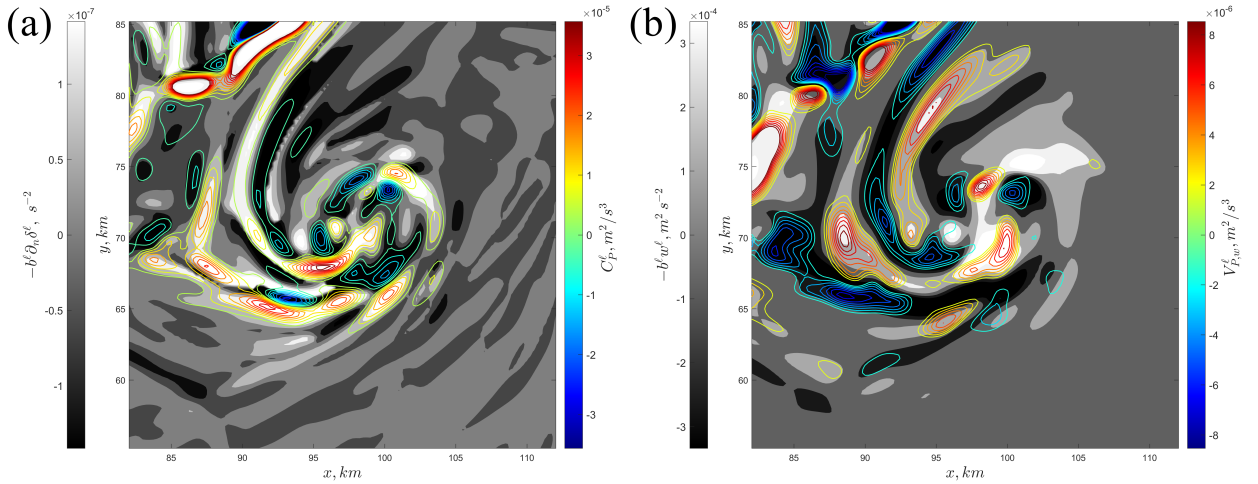


FIG. 8. Colored contours show (a) subfilter buoyancy–divergence coupling C^ℓ_P and (b) the vertical-advection contribution to the APE budget $V^\ell_{P,w}$ near a newly formed cyclone at $\ell = 4$ km on day 11. The grayscale shading shows (a) $-b^\ell \partial_n \delta^\ell$ in equation (26) and (b) $-b^\ell w^\ell$ in equation (29).

$$C^\ell_P = -b^\ell \tau^\ell(b, \delta) \tag{25}$$

represents the subfilter coupling between buoyancy and horizontal-divergence fluctuations. A positive $\tau^\ell(b, \delta)$ indicates an association of negative buoyancy with convergence and positive

buoyancy with divergence. For a resolved cold anomaly ($b^\ell < 0$), positive cold–convergence covariance gives $C_P^\ell > 0$, which removes P^ℓ. To interpret C_P^ℓ, the gradient-model approximation $\tau^\ell(b,\delta) \simeq C_G \ell^2 (\partial_j b^\ell)(\partial_j \delta^\ell)$ gives the approximation

$$C_P^\ell \simeq -C_G \ell^2 \nabla_h \left[\frac{(b^\ell)^2}{2} \right] \cdot \nabla_h \delta^\ell = -C_G \ell^2 b^\ell |\nabla_h b^\ell| \, \partial_n \delta^\ell. \tag{26}$$

The second equality uses the front-following coordinates $(\boldsymbol{n}_b, \boldsymbol{t}_b)$ defined in equation (23) and shown in figure 4.

$\partial_n \delta^\ell = \boldsymbol{n}_b \cdot \nabla_h \delta^\ell$ is the cross-frontal divergence gradient. It controls the sign of C_P^ℓ at fixed b^ℓ. For a cold anomaly ($b^\ell < 0$), $\boldsymbol{n}_b$ points from the cold/dense side toward the warm/light side. If surface convergence is preferentially concentrated on the cold side, δ^ℓ increases from its negative minimum toward the warm side, so that $\partial_n \delta^\ell > 0$. equation (26) then gives $C_P^\ell > 0$. For the distinct case of a two-flank cold filament, the same sign follows on each flank: $\boldsymbol{n}_b$ points outward from the buoyancy minimum at the cold core, while δ^ℓ increases away from a convergent minimum there, giving $\partial_n \delta^\ell > 0$ and $C_P^\ell > 0$ on both flanks. This geometry is consistent with the double-cell ageostrophic circulation of cold-filament intensification, which focuses surface convergence and downwelling near the filament core (McWilliams et al. 2009), and with the dense-side convergence in frontal secondary circulations (Garcia-Jove et al. 2022). Figure 8(a) shows that $C_P^\ell > 0$ in the cold filaments, consistent with the prediction of equation (26).

The native closure in equation (14) evaluates the horizontal flux-divergence tendency H_b' in conservative form, whereas equation (18) decomposes the horizontal advection $\mathcal{H}_{b,\mathrm{adv}}$. These two are not generally identical when the flow is horizontally divergent. Their horizontal and vertical partitions differ, although the sum $H_b' + V_b'$ reproduces the full three-dimensional advective tendency of the buoyancy anomaly. To preserve this sum while replacing its horizontal partition by equation (18), we define the effective vertical-advection tendency as

$$V_{b,\mathrm{eff}} = H_b' + V_b' - \mathcal{H}_{b,\mathrm{adv}}. \tag{27}$$

It reduces to V_b' when $H_b' = \mathcal{H}_{b,\mathrm{adv}}$ at $\delta = 0$. Using three-dimensional incompressibility in equation (13) and equation (10), this expression becomes

$$V_{b,\mathrm{eff}} = -\beta \left[wT_z - \langle wT_z \rangle_h \right] + \beta \langle \boldsymbol{u}_h \cdot \nabla_h T \rangle_h .$$

Its contribution to P^ℓ tendency is

$$\begin{aligned} V^\ell_{P,\mathrm{eff}} &\equiv b^\ell (V_{b,\mathrm{eff}})^\ell = V^\ell_{P,w} + V^\ell_{P,c} \\ V^\ell_{P,w} &= -\beta b^\ell \left[wT_z - \langle wT_z \rangle_h \right]^\ell \\ V^\ell_{P,c} &= \beta b^\ell \langle \boldsymbol{u}_h \cdot \nabla_h T \rangle_h \end{aligned} \tag{28}$$

The vertical-advection contribution $V^\ell_{P,w}$ is positive when the mean-removed, filtered vertical-advection tendency reinforces the resolved buoyancy anomaly and negative when it weakens that anomaly. Using the identity $(wT_z)^\ell = w^\ell T^\ell_z + \tau^\ell(w, T_z)$ in equation (28) gives

$$V^\ell_{P,w} = -\beta b^\ell \left[w^\ell T^\ell_z + \tau^\ell(w, T_z) - \langle wT_z \rangle_h \right] \simeq -\beta T^\ell_z b^\ell w^\ell . \tag{29}$$

The approximation requires $|\tau^\ell(w, T_z)| \ll |w^\ell T^\ell_z|$ and $|\langle wT_z \rangle_h| \ll |w^\ell T^\ell_z|$. These conditions may hold locally when T_z varies slowly across the filter footprint and the mean-removal correction is weak. Under this approximation, with z positive upward and stable stratification $T^\ell_z > 0$, cold-anomaly upwelling and warm-anomaly downwelling increase P^ℓ, whereas cold-anomaly downwelling and warm-anomaly upwelling decrease it. Figure 8(b) compares $V^\ell_{P,w}$ with $-b^\ell w^\ell$; their spatial correspondence is consistent with this interpretation. Because $\langle b^\ell \rangle_h = 0$ under mean-preserving filtering, $V^\ell_{P,c}$ makes no contribution to the horizontally averaged APE tendency, although it can modify the local budget. Its spatial structure follows b^ℓ up to a horizontally uniform factor and is not shown here.

Finally, combining equations (18) and (27) with the native closure in equation (14) gives the local budget of horizontally coarse-grained eddy available potential energy:

$$\partial_t P^\ell + \nabla_h \cdot \boldsymbol{F}^\ell_P = -\Pi^\ell_P - A^\ell_P - C^\ell_P + V^\ell_{P,\mathrm{eff}} + \mathcal{D}^\ell_P . \tag{30}$$

Here, $\mathcal{D}_P^\ell = b^\ell (D_b')^\ell$ is the diffusion contribution. Taking the horizontal average gives

$$\partial_t \left\langle P^\ell \right\rangle_h = -\left\langle \Pi_P^\ell \right\rangle_h - \left\langle A_P^\ell \right\rangle_h - \left\langle C_P^\ell \right\rangle_h + \left\langle V_{P,\mathrm{eff}}^\ell \right\rangle_h + \left\langle \mathcal{D}_P^\ell \right\rangle_h . \tag{31}$$

The horizontal transport divergence vanishes upon averaging under periodic or zero-normal-flux boundary conditions.

5. Conclusion

We have examined how mixed layer instability organizes surface KE and EAPE transfers in an idealized, freely evolving front. During the initial adjustment, broad divergent anticyclonic patches coexist with narrow convergent cyclonic filaments at the surface and near the mixed-layer base. The patches are warm and the filaments cold at the surface, whereas these thermal signatures are reversed near the mixed-layer base. Positive vorticity skewness and negative divergence skewness develop during the rapid release of frontal APE, before the vorticity medians become positive. Intense cyclonic and convergent structures thus emerge while the spatially extensive background remains predominantly anticyclonic.

This spatial contrast between convergent cyclonic filaments and divergent anticyclonic patches also organizes the surface energy pathways: cold filaments support forward KE and EAPE transfer ($\Pi_K^\ell > 0$ and $\Pi_P^\ell > 0$), whereas adjacent warm patches support inverse transfer ($\Pi_K^\ell < 0$ and $\Pi_P^\ell < 0$). Surface convergence ($\delta^\ell < 0$) squeezes the cyclonic cold filaments, concentrating velocity differences and buoyancy contrasts over progressively smaller scales. The convergent deformation does work against subfilter velocity stresses τ_{ij}^ℓ, transferring KE from the resolved flow K^ℓ to smaller scales through isotropic compression ($\Pi_{K,\mathrm{comp}}^\ell > 0$). At the same time, cross-front compression sharpens the buoyancy gradients $\nabla_h b^\ell$ and transfers EAPE P^ℓ forward through $\Pi_{P,\mathrm{div}}^\ell > 0$ in the gradient-model interpretation. Preferential cross-front compression ($\epsilon_{nn}^\ell < \epsilon_{tt}^\ell$), accompanied by along-front stretching, further favors forward deviatoric EAPE transfer ($\Pi_{P,\mathrm{dev}}^\ell > 0$). The cyclonic cold filaments therefore act as localized conduits for forward KE and EAPE cascades through submesoscale frontogenesis during MLI.

The local energy budgets distinguish these interscale transfers from resolved horizontal expansion or compression, represented by $A_K^\ell = -\delta^\ell K^\ell$ and $A_P^\ell = -\delta^\ell P^\ell$. In convergent cold filaments, $A_K^\ell > 0$ and $A_P^\ell > 0$; because these terms enter the respective budgets with minus signs, both reduce

resolved energies. The magnitude of the KE expansion or compression term, $|A_K^\ell|$, can exceed that of the KE cascade, $|\Pi_K^\ell|$. Subfilter divergence coupling has contrasting effects on the two energies. The diagnosed velocity–divergence coupling $C_K^\ell = -u_i^\ell \tau_\ell(u_i, \delta) < 0$ supplies resolved KE, whereas the buoyancy–divergence coupling $C_P^\ell = -b^\ell \tau^\ell(b, \delta) > 0$ removes resolved EAPE. Their gradient-model expressions relate these effects to the alignment of energy and divergence gradients. Near a forming cyclone, horizontal pressure-gradient work Π_a^ℓ supplies KE through inward ageostrophic motion ($\Pi_a^\ell > 0$) and removes KE through outward motion ($\Pi_a^\ell < 0$), linking local energy exchange to cyclonic spin-up and the surrounding circulation.

The EAPE formulation retains vertical advection and preserves the model's native three-dimensional temperature tendency through the effective vertical-advection contribution $V_{P,\mathrm{eff}}^\ell = V_{P,w}^\ell + V_{P,c}^\ell$. Under stable stratification ($T_z^\ell > 0$), cold-anomaly downwelling and warm-anomaly upwelling give $V_{P,w}^\ell \simeq -\beta T_z^\ell b^\ell w^\ell < 0$, reducing local EAPE. The correction $V_{P,c}^\ell$ can affect the local budget but has zero horizontal mean. The current results identify frontal convergence ($\delta^\ell < 0$) and its spatial gradients $\nabla_h \delta^\ell$ as key organizers of the distinct KE and EAPE pathways during MLI.

Data availability statement. Data availability will be specified in the final manuscript.

APPENDIX A

Gradient model

The gradient model of Clark et al. (1979) approximates the subfilter covariance $\tau^\ell(f,g) = (fg)^\ell - f^\ell g^\ell$ between two fields f and g using the resolved spatial gradients

$$\boxed{\tau^\ell(f,g) = C_G \ell^2 (\partial_j f^\ell)(\partial_j g^\ell) + O(\ell^4), \qquad C_G = \frac{1}{9}.} \tag{A1}$$

The gradient model is used throughout section 4 to interpret the coarse-grained energy-budget terms. This appendix derives the above relation, with repeated horizontal indices summed over $j = 1, 2$. The derivation establishes the coefficient for the Gaussian kernel in equation (2) and the order of the neglected terms, providing the basis for using equation (A1) in both the kinetic- and potential-energy budgets.

For a scalar field f, define the horizontal filter by

$$f^\ell(\boldsymbol{x}) = \int_{\mathbb{R}^2} G_\ell(\boldsymbol{r}) f(\boldsymbol{x}+\boldsymbol{r})\, \mathrm{d}\boldsymbol{r},$$

The two-dimensional Gaussian kernel in equation (2) is normalized, centered, symmetric, and isotropic, so that

$$\int_{\mathbb{R}^2} G_\ell(\boldsymbol{r})\, \mathrm{d}\boldsymbol{r} = 1, \qquad \int_{\mathbb{R}^2} r_j G_\ell(\boldsymbol{r})\, \mathrm{d}\boldsymbol{r} = 0. \tag{A2}$$

The second moment of the kernel is

$$\int_{\mathbb{R}^2} r_j r_k G_\ell(\boldsymbol{r})\, \mathrm{d}\boldsymbol{r} = \delta_{jk} \frac{3}{\sqrt{2\pi}\ell} \int_{-\infty}^{\infty} s^2 \exp\left(-\frac{9s^2}{2\ell^2}\right) \mathrm{d}s = \frac{\ell^2}{9}\delta_{jk}. \tag{A3}$$

Thus the dimensionless coordinate-wise second-moment coefficient for this particular definition of the filter scale is $C_G = 1/9$.

Expanding $f(\boldsymbol{x}+\boldsymbol{r})$ about $\boldsymbol{x}$ gives

$$f(\boldsymbol{x}+\boldsymbol{r}) = f + r_j\partial_j f + \frac{1}{2}r_j r_k \partial_j\partial_k f + \frac{1}{3!}r_j r_k r_m \partial_j\partial_k\partial_m f + O(|\boldsymbol{r}|^4),$$

where repeated horizontal indices are summed. Filtering this expansion with equations (A2) and (A3) eliminates all odd moments and yields

$$f^\ell = f + \frac{\ell^2}{18}\nabla_h^2 f + O(\ell^4). \tag{A4}$$

Applying equation (A4) to the product fg gives

$$(fg)^\ell = fg + \frac{\ell^2}{18}\nabla_h^2(fg) + O(\ell^4), \tag{A5}$$

whereas applying it separately to f and g gives

$$f^\ell g^\ell = fg + \frac{\ell^2}{18}\left(f\nabla_h^2 g + g\nabla_h^2 f\right) + O(\ell^4). \tag{A6}$$

The product rule

$$\nabla_h^2(fg) = f\nabla_h^2 g + g\nabla_h^2 f + 2(\partial_j f)(\partial_j g)$$

then shows, by subtracting equation (A6) from equation (A5), that $\tau^\ell(f,g) = (\ell^2/9)(\partial_j f)(\partial_j g) + O(\ell^4)$. Moreover, equation (A4) implies $\partial_j f^\ell = \partial_j f + O(\ell^2)$ and similarly for g. Replacing the unfiltered gradients by filtered gradients therefore changes only the $O(\ell^4)$ remainder and recovers equation (A1), with $C_G = 1/9$. This leading-order approximation requires sufficiently smooth fields over ℓ, approximate commutation of filtering and differentiation, and subdominant higher-order terms. For a truncated or discrete implementation of the Gaussian kernel, $C_G\ell^2$ should be evaluated from the kernel's actual coordinate-wise second moment.

References

Aluie, H., M. W. Hecht, and G. K. Vallis, 2018: Mapping the energy cascade in the north atlantic ocean: The coarse-graining approach. *J. Phys. Oceanogr.*, **48 (2)**, 225–244, https://doi.org/10.

1175/JPO-D-17-0100.1.

Barkan, R., M. J. Molemaker, K. Srinivasan, J. C. McWilliams, and E. A. D'Asaro, 2019: The role of horizontal divergence in submesoscale frontogenesis. *J. Phys. Oceanogr.*, **49 (6)**, 1593–1618, https://doi.org/10.1175/JPO-D-18-0162.1.

Boccaletti, G., R. Ferrari, and B. Fox-Kemper, 2007: Mixed layer instabilities and restratification. *J. Phys. Oceanogr.*, **37 (9)**, 2228–2250, https://doi.org/10.1175/JPO3101.1.

Brannigan, L., D. P. Marshall, A. C. Naveira Garabato, A. J. G. Nurser, and J. Kaiser, 2017: Submesoscale instabilities in mesoscale eddies. *J. Phys. Oceanogr.*, **47 (12)**, 3061–3085, https://doi.org/10.1175/JPO-D-16-0178.1.

Buckingham, C. E., and Coauthors, 2016: Seasonality of submesoscale flows in the ocean surface boundary layer. *Geophys. Res. Lett.*, **43 (5)**, 2118–2126, https://doi.org/10.1002/2016GL068009.

Callies, J., and R. Ferrari, 2013: Interpreting energy and tracer spectra of upper-ocean turbulence in the submesoscale range (1–200 km). *J. Phys. Oceanogr.*, **43 (11)**, 2456–2474, https://doi.org/10.1175/JPO-D-13-063.1.

Callies, J., R. Ferrari, J. M. Klymak, and J. Gula, 2015: Seasonality in submesoscale turbulence. *Nat. Commun.*, **6**, 6862, https://doi.org/10.1038/ncomms7862.

Callies, J., G. Flierl, R. Ferrari, and B. Fox-Kemper, 2016: The role of mixed-layer instabilities in submesoscale turbulence. *J. Fluid Mech.*, **788**, 5–41, https://doi.org/10.1017/jfm.2015.700.

Cao, H., B. Fox-Kemper, and Z. Jing, 2021: Submesoscale eddies in the upper ocean of the kuroshio extension from high-resolution simulation: Energy budget. *J. Phys. Oceanogr.*, **51 (7)**, 2181–2201, https://doi.org/10.1175/JPO-D-20-0267.1.

Capet, X., J. C. McWilliams, M. J. Molemaker, and A. F. Shchepetkin, 2008a: Mesoscale to submesoscale transition in the california current system. part I: Flow structure, eddy flux, and observational tests. *J. Phys. Oceanogr.*, **38 (1)**, 29–43, https://doi.org/10.1175/2007JPO3671.1.

Capet, X., J. C. McWilliams, M. J. Molemaker, and A. F. Shchepetkin, 2008b: Mesoscale to submesoscale transition in the california current system. part II: Frontal processes. *J. Phys. Oceanogr.*, **38 (1)**, 44–64, https://doi.org/10.1175/2007JPO3672.1.

583 Capet, X., J. C. McWilliams, M. J. Molemaker, and A. F. Shchepetkin, 2008c: Mesoscale to sub-
584 mesoscale transition in the california current system. part III: Energy balance and flux. *J. Phys.*
585 *Oceanogr.*, **38 (10)**, 2256–2269, https://doi.org/10.1175/2008JPO3810.1.

586 Clark, R. A., J. H. Ferziger, and W. C. Reynolds, 1979: Evaluation of subgrid-scale models using
587 an accurately simulated turbulent flow. *J. Fluid Mech.*, **91 (1)**, 1–16, https://doi.org/10.1017/
588 S002211207900001X.

589 D'Asaro, E. A., C. R. Lee, L. Rainville, R. R. Harcourt, and L. N. Thomas, 2011: Enhanced tur-
590 bulence and energy dissipation at ocean fronts. *Science*, **332 (6027)**, 318–322, https://doi.org/
591 10.1126/science.1201515.

592 Fox-Kemper, B., and R. Ferrari, 2008: Parameterization of mixed layer eddies. part ii: Prognosis
593 and impact. *J. Phys. Oceanogr.*, **38 (6)**, 1166–1179, https://doi.org/10.1175/2007JPO3788.1.

594 Fox-Kemper, B., R. Ferrari, and R. Hallberg, 2008: Parameterization of mixed layer eddies.
595 part i: Theory and diagnosis. *J. Phys. Oceanogr.*, **38 (6)**, 1145–1165, https://doi.org/10.1175/
596 2007JPO3792.1.

597 Fox-Kemper, B., and Coauthors, 2011: Parameterization of mixed layer eddies. III: Implemen-
598 tation and impact in global ocean climate simulations. *Ocean Modelling*, **39 (1–2)**, 61–78,
599 https://doi.org/10.1016/j.ocemod.2010.09.002.

600 Garcia-Jove, M., B. Mourre, N. D. Zarokanellos, P. F. J. Lermusiaux, D. L. Rudnick, and J. Tintoré,
601 2022: Frontal dynamics in the Alboran Sea: 2. processes for vertical velocities development. *J.*
602 *Geophys. Res. Oceans*, **127**, e2021JC017 428, https://doi.org/10.1029/2021JC017428.

603 Haine, T. W. N., and J. Marshall, 1998: Gravitational, symmetric, and baroclinic instabil-
604 ity of the ocean mixed layer. *J. Phys. Oceanogr.*, **28 (4)**, 634–658, https://doi.org/10.1175/
605 1520-0485(1998)028<0634:GSABIO>2.0.CO;2.

606 Haney, S., B. Fox-Kemper, K. Julien, and A. Webb, 2015: Symmetric and geostrophic instabilities
607 in the wave-forced ocean mixed layer. *J. Phys. Oceanogr.*, **45 (12)**, 3033–3056, https://doi.org/
608 10.1175/JPO-D-15-0044.1.

609 Luo, Y., and J. Callies, 2023: Vertical exchange induced by mixed layer instabilities. *J. Phys.*
610 *Oceanogr.*, **53 (12)**, 2701–2716, https://doi.org/10.1175/JPO-D-23-0059.1.

Mahadevan, A., 2016: The impact of submesoscale physics on primary productivity of plankton. *Annu. Rev. Mar. Sci.*, **8**, 161–184, https://doi.org/10.1146/annurev-marine-010814-015912.

Mahadevan, A., and A. Tandon, 2006: An analysis of mechanisms for submesoscale vertical motion at ocean fronts. *Ocean Modelling*, **14 (3–4)**, 241–256, https://doi.org/10.1016/j.ocemod.2006.05.006.

Marshall, J., A. Adcroft, C. Hill, L. Perelman, and C. Heisey, 1997a: A finite-volume, incompressible Navier–Stokes model for studies of the ocean on parallel computers. *J. Geophys. Res.*, **102 (C3)**, 5753–5766, https://doi.org/10.1029/96JC02775.

Marshall, J., C. Hill, L. Perelman, and A. Adcroft, 1997b: Hydrostatic, quasi-hydrostatic, and nonhydrostatic ocean modeling. *J. Geophys. Res.*, **102 (C3)**, 5733–5752, https://doi.org/10.1029/96JC02776.

McWilliams, J. C., 2016: Submesoscale currents in the ocean. *Proc. R. Soc. A*, **472 (2189)**, 20160 117, https://doi.org/10.1098/rspa.2016.0117.

McWilliams, J. C., F. Colas, and M. J. Molemaker, 2009: Cold filamentary intensification and oceanic surface convergence lines. *Geophys. Res. Lett.*, **36**, L18 602, https://doi.org/10.1029/2009GL039402.

Mensa, J. A., Z. Garraffo, A. Griffa, T. M. Özgökmen, A. Haza, and M. Veneziani, 2013: Seasonality of the submesoscale dynamics in the gulf stream region. *Ocean Dynamics*, **63 (8)**, 923–941, https://doi.org/10.1007/s10236-013-0633-1.

Molemaker, M. J., J. C. McWilliams, and I. Yavneh, 2005: Baroclinic instability and loss of balance. *J. Phys. Oceanogr.*, **35 (9)**, 1505–1517, https://doi.org/10.1175/JPO2770.1.

Nagai, T., A. Tandon, and D. L. Rudnick, 2006: Two-dimensional ageostrophic secondary circulation at ocean fronts due to vertical mixing and large-scale deformation. *J. Geophys. Res. Oceans*, **111**, C09 038, https://doi.org/10.1029/2005JC002964.

Naveira Garabato, A. C., X. Yu, J. Callies, R. Barkan, K. L. Polzin, E. E. Frajka-Williams, C. E. Buckingham, and S. M. Griffies, 2022: Kinetic energy transfers between mesoscale and

submesoscale motions in the open ocean's upper layers. *J. Phys. Oceanogr.*, **52 (1)**, 75–97, https://doi.org/10.1175/JPO-D-21-0099.1.

Omand, M. M., E. A. D'Asaro, C. M. Lee, M. J. Perry, N. Briggs, I. Cetinić, and A. Mahadevan, 2015: Eddy-driven subduction exports particulate organic carbon from the spring bloom. *Science*, **348 (6231)**, 222–225, https://doi.org/10.1126/science.1260062.

Roullet, G., and P. Klein, 2010: Cyclone-anticyclone asymmetry in geophysical turbulence. *Phys. Rev. Lett.*, **104 (21)**, 218 501, https://doi.org/10.1103/PhysRevLett.104.218501.

Sasaki, H., P. Klein, B. Qiu, and Y. Sasai, 2014: Impact of oceanic-scale interactions on the seasonal modulation of ocean dynamics by the atmosphere. *Nat. Commun.*, **5**, 5636, https://doi.org/10.1038/ncomms6636.

Schubert, R., J. Gula, R. J. Greatbatch, B. Baschek, and A. Biastoch, 2020: The submesoscale kinetic energy cascade: Mesoscale absorption of submesoscale mixed layer eddies and frontal downscale fluxes. *J. Phys. Oceanogr.*, **50 (9)**, 2573–2589, https://doi.org/10.1175/JPO-D-19-0311.1.

Shcherbina, A. Y., E. A. D'Asaro, C. M. Lee, J. M. Klymak, M. J. Molemaker, and J. C. McWilliams, 2013: Statistics of vertical vorticity, divergence, and strain in a developed submesoscale turbulence field. *Geophys. Res. Lett.*, **40 (17)**, 4706–4711, https://doi.org/10.1002/grl.50919.

Srinivasan, K., R. Barkan, and J. C. McWilliams, 2023: A forward energy flux at submesoscales driven by frontogenesis. *J. Phys. Oceanogr.*, **53 (1)**, 287–305, https://doi.org/10.1175/JPO-D-22-0001.1.

Steinberg, J. M., S. T. Cole, K. Drushka, and R. P. Abernathey, 2022: Seasonality of the mesoscale inverse cascade as inferred from global scale-dependent eddy energy observations. *J. Phys. Oceanogr.*, **52 (8)**, 1677–1691, https://doi.org/10.1175/JPO-D-21-0269.1.

Su, Z., J. Wang, P. Klein, A. F. Thompson, and D. Menemenlis, 2018: Ocean submesoscales as a key component of the global heat budget. *Nat. Commun.*, **9**, 775, https://doi.org/10.1038/s41467-018-02983-w.

Tandon, A., and C. Garrett, 1994: Mixed layer restratification due to a horizontal density gradient. *J. Phys. Oceanogr.*, **24 (6)**, 1419–1424, https://doi.org/10.1175/1520-0485(1994)024<1419:MLRDTA>2.0.CO;2.

Tandon, A., and C. Garrett, 1995: Geostrophic adjustment and restratification of a mixed layer with horizontal gradients above a stratified layer. *J. Phys. Oceanogr.*, **25 (9)**, 2229–2241, https://doi.org/10.1175/1520-0485(1995)025<2229:GAAROA>2.0.CO;2.

Thomas, L. N., and R. Ferrari, 2008: Friction, frontogenesis, and the stratification of the surface mixed layer. *J. Phys. Oceanogr.*, **38 (11)**, 2501–2518, https://doi.org/10.1175/2008JPO3797.1.

Thompson, A. F., A. Lazar, C. E. Buckingham, A. C. Naveira Garabato, G. M. Damerell, and K. J. Heywood, 2016: Open-ocean submesoscale motions: A full seasonal cycle of mixed layer instabilities from gliders. *J. Phys. Oceanogr.*, **46 (4)**, 1285–1307, https://doi.org/10.1175/JPO-D-15-0170.1.

Wang, T., R. Barkan, J. C. McWilliams, and M. J. Molemaker, 2021: Structure of submesoscale fronts of the mississippi river plume. *J. Phys. Oceanogr.*, **51 (4)**, 1113–1131, https://doi.org/10.1175/JPO-D-20-0191.1.

Whitt, D. B., and J. R. Taylor, 2017: Energetic submesoscales maintain strong mixed layer stratification during an autumn storm. *J. Phys. Oceanogr.*, **47 (10)**, 2419–2427, https://doi.org/10.1175/JPO-D-17-0130.1.

Yang, Y., J. C. McWilliams, X. S. Liang, H. Zhang, R. H. Weisberg, Y. Liu, and D. Menemenlis, 2021: Spatial and temporal characteristics of the submesoscale energetics in the gulf of mexico. *J. Phys. Oceanogr.*, **51 (2)**, 475–489, https://doi.org/10.1175/JPO-D-20-0247.1.

Yu, X., R. Barkan, and A. C. Naveira Garabato, 2024: Intensification of submesoscale frontogenesis and forward energy cascade driven by upper-ocean convergent flows. *Nat. Commun.*, **15**, 9214, https://doi.org/10.1038/s41467-024-53551-4.

Yu, X., A. C. Naveira Garabato, A. P. Martin, C. E. Buckingham, L. Brannigan, and Z. Su, 2019: An annual cycle of submesoscale vertical flow and restratification in the upper ocean. *J. Phys. Oceanogr.*, **49 (6)**, 1439–1461, https://doi.org/10.1175/JPO-D-18-0253.1.